

# Simulation of Semivolatile Organic Compound Microtransport at Different Time Scales in Airborne Diesel Soot Particles

MICHAEL R. STROMMEN AND  
RICHARD M. KAMENS\*

*Department of Environmental Sciences and Engineering,  
The University of North Carolina at Chapel Hill, CB 7400,  
Rosenau Hall, Chapel Hill, North Carolina 27599-7400*

The microtransport of polycyclic aromatic hydrocarbons (PAHs) in airborne diesel soot particles over time scales ranging from 0.18 s to 11.9 h was studied via a smog chamber experiment and simulated using radial diffusion models. The sorption of the PAHs by particles over long time periods (i.e., minutes to hours) was studied by monitoring the gas and particle-phase concentrations in the chamber over the course of the experiment (11.9 h). Additionally, the desorption of PAHs from particles over short time scales (i.e., tenths of seconds to several seconds) was observed by passing the aerosol through a large gas-phase stripping device and a sampling denuder to remove the aerosol's gas phase, thus causing the PAHs to desorb from the particles. The results of each experimental test were compared to simulation results using a one-layer model and four dual-impedance radial diffusion models. The dual-impedance models were able to closely reproduce the experimental results of each test, while the one-layer model produced poor fits to the experimental data, especially for the rapid desorption tests. The low values of the resulting optimized apparent diffusion coefficients ( $\sim 10^{-19}$ – $10^{-11}$  cm<sup>2</sup>/s) indicate significant impedance to microtransport beyond simple free-liquid diffusion. The mechanisms responsible for these impedances are explored. The results of this study indicate that a dual-impedance radial diffusion model is a useful tool for predicting the microtransport of PAHs in diesel soot particles (and probably other types of carbonaceous particles containing a significant organic fraction) over a wide range of time scales.

## Introduction

Recent epidemiological studies show that exposure to elevated levels of atmospheric particulate matter is associated with a significant increase in mortality and morbidity risk in humans (1, 2). Although the causes of these responses are not well understood, many researchers believe the toxicological effects of organic constituents sorbed to inhaled particulate matter may be partially responsible. Many of the most harmful organic constituents, such as polycyclic aromatic hydrocarbons (PAHs), polychlorinated biphenyls, and chlorinated dibenzodioxins and dibenzofurans, have vapor pressures in the range of  $10^{-2}$ – $10^{-7}$  Torr at ambient conditions. As such, these semivolatile organic compounds

(SOCs) demonstrate significant partitioning between the gas phase and sorption in and on atmospheric particulate matter (3–6). Since the atmospheric fate of a compound is strongly dependent on the phase in which it exists (7), knowledge of gas–particle partitioning is critical to understanding the fate of these toxic compounds in the environment. Furthermore, since gas–particle partitioning equilibrium is not always achieved in real atmospheres (8, 9), it is important to understand and quantify the dynamics of gas–particle partitioning, which is controlled by microtransport (i.e., diffusional) processes in the particles.

Radial diffusion models have been used by numerous researchers over the past 20 years to study the microtransport of contaminants in soil particles (10–15). However, only a few studies have investigated their use in simulating the microtransport of constituents in atmospheric particulate matter (16–18), and each of these models included only one level of impedance in the particles. Strommen and Kamens (19) recently proposed a model that included two levels of diffusional impedance (dual-impedance model) to simulate the rapid SOC sorption by particles observed during the first seconds to minutes in smog chamber experiments as well as the slower rate of sorption observed over the course of hours. They used this model to closely reproduce the observed sorption of deuterated PAHs by airborne diesel and wood soot particles. However, the smog chamber experiments used in these studies were not well suited to precisely resolve the extremely rapid sorption of gas-phase PAHs by diesel soot particles early in the experiment. Accordingly, to provide a rigorous validation of the dual-impedance model (19), it must be challenged against experimental data that quantify the rates of SOC microtransport in combustion particles over time scales ranging from tenths of a second to hours.

In this work, the microtransport of SOCs in airborne diesel soot particles was studied by comparing experimental data on the rates of sorption and desorption of PAHs over time scales ranging from tenths of seconds to hours with simulation results from radial diffusion models.

## Experimental Section

**Experimental Setup.** The experimental work was conducted under darkness at the University of North Carolina outdoor chamber facility (18, 19). A hot injector operating at  $\sim 200$  °C was used to introduce gas-phase deuterated fluorene, phenanthrene, fluoranthene, and benz[a]anthracene (Cambridge Isotope Laboratories, Andover, MA) into a 190 m<sup>3</sup> Teflon-film chamber (20). Deuterated compounds were used to distinguish them from their hydrogenated analogues, which are products of the combustion process. Diesel soot was then added for 3 min directly from a 1980 Mercedes Benz 300 SD engine operating at 2000 rpm. Over the course of the 11.9-h experiment, the total suspended particulate (TSP) concentration ranged from 3100 to 410  $\mu\text{g}/\text{m}^3$ .

A schematic of the experimental setup is shown in Figure 1, and the sampling events are summarized in Table 1. The rate of SOC microtransport in the airborne diesel soot particles was explored at three general time scales. First, it was studied at time scales of minutes to hours by measuring the sorption of deuterated PAH by particles in the chamber. This was accomplished by measuring the particle-phase concentrations in the chamber over the course of the experiment.

Second, the rate of PAH microtransport was studied at time scales of seconds by drawing the aerosol from the chamber through a transfer pipe and a large gas-phase stripping device (LGPS) (21) and comparing measured particle-phase PAH concentrations in the chamber vs

\* Corresponding author phone: (919)966-5452; fax: (919)966-7911; e-mail: kamens@unc.edu.

TABLE 1. Sampling Events<sup>a</sup>

sampling event	time after diesel soot injection (h)	chamber samples		LGPS samples					
		FFD sample <sup>b</sup>	DFD sample ( <i>t</i> in top denuder, s)	upstream		downstream		<i>t</i> in transfer pipe (s)	<i>t</i> in transfer pipe + LGPS (s)
				FFD sample <sup>b</sup>	DFD sample <sup>c</sup>	FFD sample <sup>b</sup>	DFD sample <sup>c</sup>		
chamber 1	0.14	X	X (0.37)						
chamber 2	0.23	X	X (0.36)						
chamber 3	0.47	X	X (0.37)						
LGPS 1	1.96	X	X (0.38)		X		X	25.9	33.1
LGPS 2	3.48	X	X (0.38)		X		X	9.9	12.6
LGPS 3	5.11	X	X (0.38)		X		X	5.6	7.1
LGPS 4	6.74	X		XX <sup>d</sup>		XX <sup>d</sup>		25.9	33.1
chamber 4	8.14	XXXX <sup>e</sup>							
chamber 5	9.48	X	X (1.13)						
chamber 6	10.79	X	X (0.30)						
chamber 7	11.88	X	X (0.18)						

<sup>a</sup> All samples were collected for 20 min except chamber 1 and chamber 2 samples, which were collected for 10 min. <sup>b</sup> Collected at 15.0 (±0.5) L/min unless otherwise noted. <sup>c</sup> Collected at 15.0 (±0.7) L/min. <sup>d</sup> In this sampling event, FFD samples were collected simultaneously at different flow rates upstream and downstream of the LGPS to test PAH desorption from particles collected on the front filters. The upstream samples were collected at 15.1 and 24.9 L/min, and the downstream samples were collected at 14.7 and 23.0 L/min. <sup>e</sup> In this sampling event, four FFD samples were collected simultaneously at different flow rates (4.8, 16.9, 23.7, and 35.7 L/min) from the chamber to test PAH desorption from particles collected on the front filters.

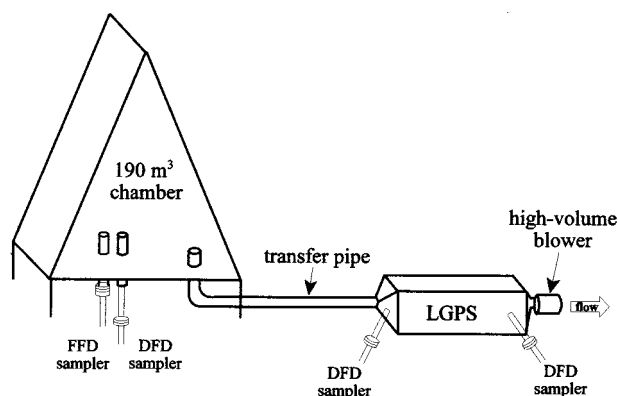


FIGURE 1. Experimental setup (not to scale).

upstream of the LGPS vs downstream of the LGPS (Figure 1). As the aerosol moved through the transfer pipe and LGPS, between 39% and 68% of the gas-phase PAH mass was removed by adsorption to the walls of the pipe, and between 60% and 99% of the gas-phase PAH mass entering the LGPS was adsorbed by the stripping units in the LGPS. However, comparison of TSP, particle size distribution, and particle number concentration in the chamber vs upstream of the LGPS vs downstream of the LGPS indicated that particle losses in the transfer pipe and LGPS were insignificant. This loss of gas-phase PAHs caused desorption of PAHs from the particles in both the transfer pipe and LGPS as the aerosol attempted to establish equilibrium gas-particle partitioning. The amount of PAH desorption in the transfer pipe and LGPS was measured by comparing the particle-phase PAH concentrations in the chamber vs upstream of the LGPS and upstream of the LGPS vs downstream of the LGPS, respectively. The LGPS was similar to the device described by Kamens and Coe (21). It is designed to remove gas-phase constituents using two stripper units, each consisting of 55 parallel carbon-impregnated quartz fiber filters (16.5 cm × 24.4 cm × 0.05 cm, Schleicher and Schuell No. 508, Keene, NH). Modifications to the LGPS from the Kamens and Coe design (21) were made to improve the uniformity of the flow velocity distribution in the unit. These included the replacement of the flow straightener with a perforated diffusion plate and the addition of a 4.5 cm diameter perforated disk placed perpendicular to the flow in the upstream expansion space. Uniformity of the flow velocity distribution was verified

using a thermo anemometer (model 8565, Alnor Instrument Co., Skokie, IL). Flow rates in the LGPS were determined by measuring the pressure drop across an orifice on the high-volume blower, which was calibrated against a chain-compensated spirometer (Warren E. Collins, Inc., Braintree, MA). The LGPS was attached to the chamber via 6.5 m of 7.4 cm diameter aluminum piping (the transfer pipe). Flow in the transfer pipe ranged from laminar (Reynolds number,  $Re = 1200$ ) to turbulent ( $Re = 5700$ ) at the different flow rates used in the experiment. Flow in the LGPS was laminar at all experimental flow rates ( $Re = 250-1100$ ). The LGPS and transfer pipe were verified to be leak-free by introducing nitric oxide (NO) into the chamber, drawing the atmosphere through the LGPS, and comparing measured NO concentrations in the chamber vs upstream of the LGPS vs downstream of the LGPS. A Monitor Labs 8440E chemiluminescent NO<sub>x</sub> analyzer (Englewood, CO) was used for NO measurements.

Third, the rate of PAH microtransport was studied at time scales of  $\leq 1$  s by drawing the aerosol from the chamber through a 37-cm annular sampling denuder and measuring PAH desorption from the particles by comparing the particle-phase PAH concentration obtained downstream of the denuder to that obtained directly from the chamber. As shown in Figure 1, this was accomplished by collecting two chamber samples simultaneously, one with a filter-filter-denuder (FFD) sampling train and one with a denuder-filter-denuder (DFD) sampling train, and comparing the measured particle-phase PAH concentrations. As the aerosol moved through the top denuder of the DFD system, >99% of the gas-phase PAHs was adsorbed by the denuder walls, while <2% of the particles was lost. This caused a desorption of PAHs from the particles as the aerosol attempted to establish equilibrium gas-particle partitioning. Thus, the amount of PAH desorption from the particles was obtained by comparing the particle-phase PAH concentration in the chamber (obtained using the FFD system) vs the particle-phase PAH concentration measured with the DFD system.

**Sampling.** Samples were collected using two sampling trains: (a) a FFD system and (b) a DFD system. The FFD system was used to measure gas- and particle-phase PAH concentrations in the chamber. The front filter measured particle-phase PAH and TSP concentrations, and the denuder measured gas-phase PAH concentrations. The backup filter was used to quantify adsorption of gas-phase PAH on the filter material. This was necessary because significant PAH mass was observed on the backup filters even though the

front filters were ~100% efficient in collecting particles (22). This indicates that gas-phase PAHs were being adsorbed by the filter material (22, 23). Since the two filters were identical, this suggests that gas-phase PAHs were also adsorbed on the front filter and thus were incorrectly categorized as being particle-phase. The magnitude of this artifact and the method used to correct the data are discussed in Appendix 1 (see Supporting Information).

The DFD system was used for two purposes. First, as discussed previously, it was used to study PAH desorption from the particles as the aerosol passed through the top denuder. Second, the DFD system was used to measure gas- and particle-phase PAH concentrations upstream and downstream of the LGPS. PAH mass collected by the top denuder was considered to be gas-phase, and the sum of the PAH mass collected on the filter and by the bottom denuder was considered to be particle-phase (19). This system was used rather than the FFD system at these sampling locations because significant desorption of PAHs from the particles collected on the front filter of the FFD system is expected. This occurs because the particles collected on this filter are exposed to low gas-phase PAH concentrations due to removal in the transfer pipe and LGPS. This causes a release of PAHs from the particles collected on the filter in an attempt to obtain gas-particle equilibrium. This was verified in sampling event LGPS 4 (Table 1) in which two FFD samplers were run simultaneously at different flow rates both upstream and downstream of the LGPS. The results showed lower particle-phase PAH concentrations for the system run at a higher flow rate for both the upstream and downstream samples. This suggests that the PAHs were desorbing from the particles collected on the front filter of the FFD system. Conversely, in the DFD system, the main artifact of concern is the desorption of PAHs from the particles as the aerosol moves through the top denuder (in fact, we use this system to study PAH desorption from particles over short time scales as discussed above). In this case, however, the particles are sampled immediately after exiting the transfer pipe or LGPS in which they resided in a gas-phase-poor environment for between 5.6 and 33.1 s. Accordingly, significant PAH mass had desorbed from the particles, and the additional PAH desorption from particles in the top denuder of the DFD sampling train (residence time,  $t_r = 0.37 \pm 0.1$  s) is not expected to be significant.

The denuders were 2.4 cm in diameter, contained five annular channels separated by 0.1 cm spaces (University Research Glassware, Carborro, NC), and were coated on the glass interior surfaces with XAD-4 resin (24). The downstream denuder in the DFD train was 24 cm in length, and the denuder in the FFD train and the top denuder in the DFD train were 37 cm long. The filters were 47 mm in diameter and composed of glass fibers impregnated with Teflon (T60A20, Pallflex Products Corp., Putnam, CT). Flow measurements were made using Schlumberger dry test meters (New York, NY) and Tylan mass flow meters (Torrence, CA). Each was calibrated against a chain-compensated spirometer (Warren E. Collins, Inc., Braintree, MA). The efficiency of the denuders for capturing each of the target gas-phase PAHs was verified to be >99%. The filters were ~100% efficient in capturing diesel particulate matter (22). These sampling systems have been characterized and described in greater detail previously (20, 25).

**Other Measurements.** Temperature and humidity were measured using a thermistor and a light-scattering dew point hygrometer (EG&G model 880, Waltham, MA), respectively. The temperature ranged from 15 to 10 °C, and the relative humidity ranged from 55 to 70%. Particle number and size distribution were measured using an electrical aerosol size analyzer (TSI Incorporated, model 3030, St. Paul, MN). Particle number was also measured using an Environment

One Rich 100 condensation nuclei monitor (Schenectady, NY).

**Sample Analysis.** The sample preparation and analysis techniques are described in detail elsewhere (19). In brief, denuders were extracted within 5 min of sampling using three ~50-mL aliquots of a 20:30:50 mixture of optima grade dichloromethane:acetone:hexane (Fisher Scientific, Fair Lawn, NJ). The extracts were immediately placed in stoppered round-bottom flasks. Extracts were concentrated to ~5 mL using rotary evaporation and to ~100  $\mu$ L using a gentle, dry nitrogen stream.

Filters were removed from the holders, weighed, and placed in amber glass jars with Teflon-lined lids at ~0 °C. Filters were Soxhlet extracted for 3 h using the solvent mixture listed above. We have verified that a 3-h extraction removes >99% of the mass obtained from an 8-h extraction for the PAHs of interest for this study. Filters were reweighed after extraction to determine the fraction of extractable particle mass, which ranged from 0.30 to 0.51 in this study. For diesel soot, we assume this value is equal to the mass fraction of organic material in the particles,  $f_{om}$ . All mass measurements were conducted using a Sartorius analytical balance (sensitivity =  $\pm 5$   $\mu$ g, model 4503, Göttingen, Germany).

An internal standard containing acenaphthene- $d_{10}$  and pyrene- $d_{10}$  was added to the denuders and filters prior to extraction to obtain analyte concentrations as described by Kirchmer et al. (26). Samples were analyzed with a Hewlett-Packard (HP) 5890 series II gas chromatograph equipped with an HP 5971A mass selective detector and a J&W DB-5ms fused silica column (30 m, 0.25 mm i.d., 0.5  $\mu$ m film). Samples were analyzed in selected ion monitoring mode for enhanced sensitivity.

Analytical precision was determined by multiple analyses of individual samples. The relative standard deviations (RSD) were as follows: fluorene- $d_{10}$ , 1.1%; phenanthrene- $d_{10}$ , 0.8%; fluoranthene- $d_{10}$ , 0.8%; and benz[a]anthracene- $d_{12}$ , 3.9%. Sample precision was determined by analyzing multiple chamber samples taken simultaneously. The RSD for gas- and particle-phase concentrations, respectively, were as follows: fluorene- $d_{10}$ , 11% and 15%; phenanthrene- $d_{10}$ , 6% and 10%; fluoranthene- $d_{10}$ , 5% and 4%; and benz[a]anthracene- $d_{12}$ , 30% and 6%. The RSD for TSP measurements was 1.2%.

## Model Development

The radial diffusion model developed for this work is described in detail in a previous study (19). In summary, the model simulates the diffusion of analytes in the radial direction in spherical particles by solving Fick's second law:

$$\frac{\partial C}{\partial t} = D_a \left[ \frac{\partial^2 C}{\partial r^2} + \left( \frac{2}{r} \right) \frac{\partial C}{\partial r} \right] \quad (1)$$

where  $C$  (ng/cm<sup>3</sup> of organic material) is the concentration of the analyte at distance  $r$  (cm) from the center of the particle, and  $D_a$  (cm<sup>2</sup>/s) is the apparent diffusion coefficient. Different  $D_a$  values may be used in different regions (layers) of the model particle. In this work, one- and two-layer (dual-impedance) models were used. In the dual-impedance models, the boundary condition at the interface of the two layers is

$$D_{a,1} \frac{\partial C_1}{\partial r} = D_{a,2} \frac{\partial C_2}{\partial r} \quad (2)$$

where  $C_1$  (ng/cm<sup>3</sup> particle organic material) is the concentration adjacent to the layer 1/layer 2 interface on the layer 1 side, and  $C_2$  (ng/cm<sup>3</sup> of organic material) is the concentration adjacent to the interface on the layer 2 side. At the surface of the particle, the boundary condition is (27)



$$-D_a \frac{\partial C}{\partial r} = \alpha(C_s - C_o) \quad (3)$$

where  $C_s$  (ng/cm<sup>3</sup> of organic material) is the concentration of the analyte immediately below the surface of the particle,  $C_o$  (ng/cm<sup>3</sup> of organic material) is the concentration of the analyte required to maintain equilibrium with the gas phase, and  $\alpha$  (cm/s) is the surface mass transfer coefficient. As in our previous work (19), surface mass transfer appeared not to be rate limiting at the time scales considered in this study. Accordingly,  $\alpha$  was set at a high, non-rate-limiting value ( $\alpha = 1 \times 10^{-4}$  cm/s) for all simulations.

The value of  $C_o$  in eq 3 is determined by

$$C_o(t) = \frac{K_p(t) C_g(t) \rho_{org}}{f_{om}(t)} \quad (4)$$

where  $K_p$  (mg of particle/m<sup>3</sup> of sample) is the gas-particle equilibrium partition coefficient (28),  $C_g$  (ng/m<sup>3</sup> of sample) is the analyte gas-phase concentration,  $\rho_{org}$  (mg/cm<sup>3</sup>) is the density of the particle organic material, and  $f_{om}$  (mg of organic material/mg of particle) is the mass fraction of organic material in the particles.

The model discretizes the particles into a series of concentric spheres (nodes) spaced at equal distances and implements a finite-difference method of lines technique (29) to provide estimates for eq 1 at each node and eqs 2 and 3 at the boundaries. This produces a system of differential algebraic equations (DAEs) that are solved using the DAE package, DDASPK (29, 30).

The model accounts for temporal changes in the following input parameters: particle size distribution, particle number, TSP,  $f_{om}$ ,  $C_g$ ,  $K_p$ , and temperature. Data for each of these parameters, except  $K_p$ , were obtained from measurements in the present study.  $K_p$  values were calculated as a function of temperature by a semi-empirical relationship developed from smog chamber data of previous diesel soot experiments as described in Appendix 2 (see Supporting Information). Other inputs include the densities of the liquid and solid portions of the particle that were obtained from diesel soot characterization studies (31, 32). The model can accommodate abrupt changes in gas-phase analyte concentration such as those experienced as the aerosol enters the transfer pipe, LGPS, or sampling denuder. The model output is the particle-phase concentration of an analyte at any point in any particle (or the total particle-phase concentration in the system) at any time. The model also includes a Levenberg-Marquardt routine (33) to allow optimization of select input parameters, such as apparent diffusion coefficients, via multiple simulations.

## Results and Discussion

Four tests were experimentally run and numerically simulated to study the rate of PAH sorption and desorption by diesel soot particles at different time scales:

(a) Sorption of PAHs by particles over long (i.e., minutes to hours) time scales. This was accomplished by measuring and simulating the sorption of deuterated PAHs by particles in the chamber over the course of the 11.9-h experiment.

(b) Desorption of PAHs from the particles as they pass through the transfer pipe and LGPS. As the aerosol passed through the transfer pipe and LGPS, a significant fraction of the gas-phase constituents was removed, thus creating a gas-phase-poor environment. PAHs then desorbed from the particles in an attempt to establish gas-particle equilibrium. The amount of desorption was experimentally studied and simulated at different residence times in the transfer pipe and LGPS ( $t_r = 5.6$ –33.1 s) by changing the flow rate through the system.

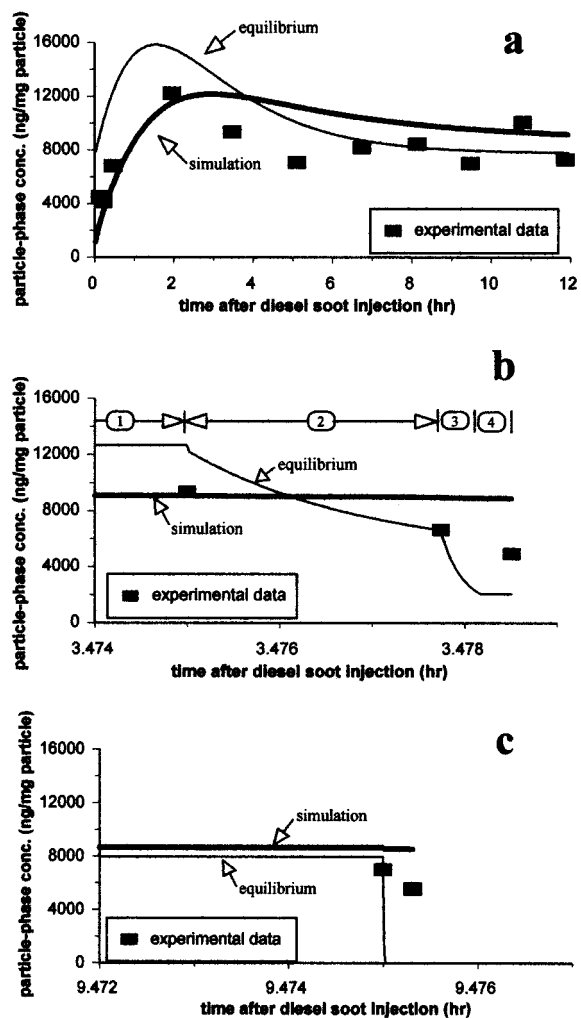


FIGURE 2. Experimental vs simulation results for fluoranthene- $d_{10}$  using the one-layer model.  $D_a = 2.2 \times 10^{-16}$  cm<sup>2</sup>/s. (a) Chamber data. (b) LGPS data. Desorption from particles in (1) chamber, (2) transfer pipe ( $t_r = 9.9$  s), (3) stripping device ( $t_r = 1.6$  s), and (4) back of stripping device housing ( $t_r = 1.2$  s). (c) Desorption from particles in a sampling denuder ( $t_r = 1.13$  s).

(c) Desorption of PAHs from particles as they pass through a sampling denuder at different flow rates. As the aerosol passed through the top denuder of the DFD sampling train, PAHs desorbed from the particles to compensate for gas-phase losses. This is similar to item b above except the time scale is shorter. The flow rate was varied such that the residence time in the sampling denuder ranged from 0.18 to 1.13 s.

(d) Desorption of PAHs from the particles as they pass through a sampling denuder at a given flow rate. This is the same as item c above except that the samples were taken over the course of the experiment at a constant flow rate ( $t_r$  in sampling denuder =  $0.37 \pm 0.1$  s).

Apparent diffusion coefficients were obtained for each compound and each model by optimization to the experimental data over all tests and samples discussed above [i.e., for a given PAH and a given model particle, a single  $D_a$  value (for the one-layer model) and single  $D_{a,1}$  and  $D_{a,2}$  values (for each dual-impedance model) were obtained that produced the best fits to the experimental data for all samples taken for tests a–d above].

**Sorption of PAHs by Particles over Long Time Scales.** Samples were periodically drawn from the chamber over the course of the experiment for this test (each sampling event

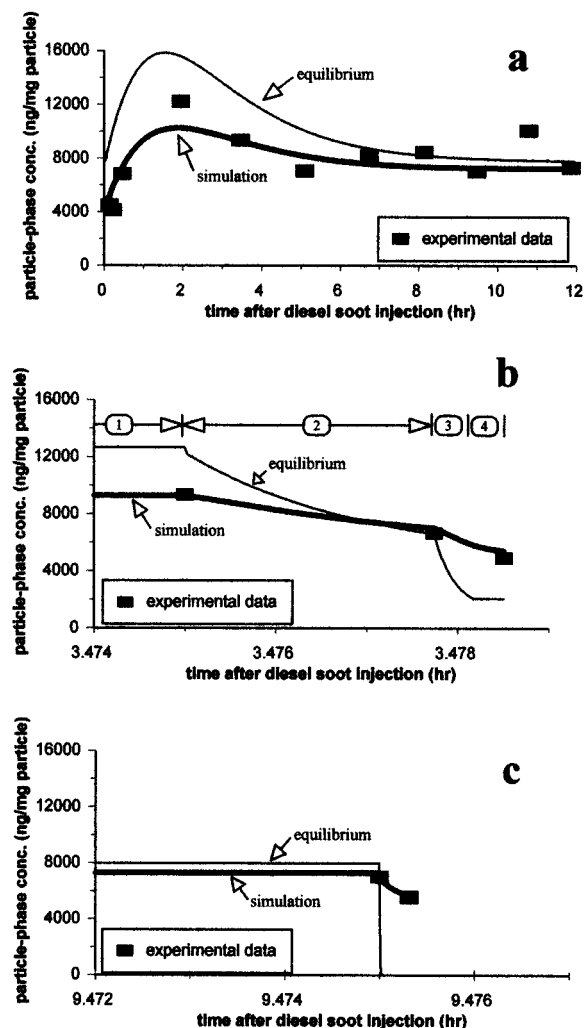


FIGURE 3. Experimental vs simulation results for fluoranthene- $d_{10}$  using a dual-impedance model.  $D_{a,1} = 1.7 \times 10^{-13} \text{ cm}^2/\text{s}$ ,  $D_{a,2} = 2 \times 10^{-16} \text{ cm}^2/\text{s}$ . See Figure 2a–c for individual captions.

in Table 1). A comparison of the experimental vs model particle-phase fluoranthene- $d_{10}$  results is shown in Figures 2a and 3a for the one-layer and dual-impedance models, respectively. Note that a better fit is obtained for the dual-impedance model than the one-layer model. The dual-impedance model results for fluorene- $d_{10}$ , phenanthrene- $d_{10}$ , and benz[a]anthracene- $d_{12}$  are shown in Figures A3-1a, A3-2a, and A3-3a of Appendix 3 (see Supporting Information). The apparent diffusion coefficients were obtained by optimization. However, using only the chamber data (i.e., Figures 3a, A3-1a, A3-2a, and A3-3a), the outer-layer apparent diffusion coefficient,  $D_{a,1}$ , for the dual-impedance model did not optimize to a specific value but to a value of  $\geq 10^{-14} \text{ cm}^2/\text{s}$  for each compound. This indicates that the experimental method is not sensitive enough to elucidate specific  $D_{a,1}$  values (i.e., samples cannot be taken quickly enough from the chamber at the beginning of the experiment to quantify the rapid initial rate of PAH sorption by the particles). As such, the desorption tests discussed below in which the time scales are as low as tenths of seconds must be used to obtain  $D_{a,1}$  values.

**Desorption of PAHs from the Particles as They Pass through the Transfer Pipe and LGPS.** Gas- and particle-phase PAH concentrations were measured in the chamber, upstream of the LGPS, and downstream of the LGPS for this test (sampling events LGPS 1–3 in Table 1). Different flow rates through the LGPS system were used for each sampling event to study PAH desorption from the particles at residence

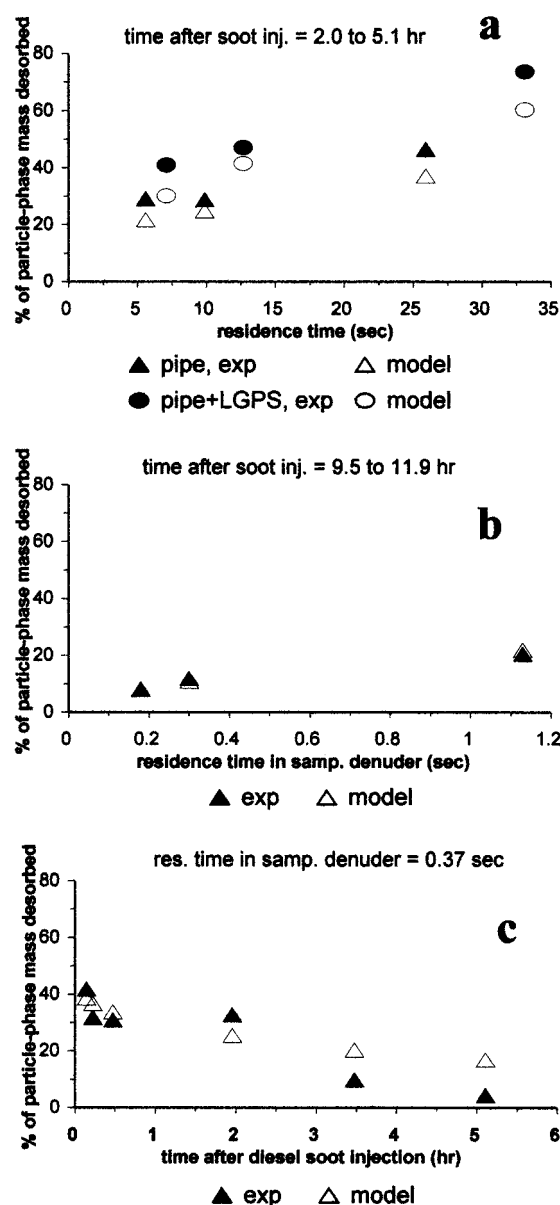


FIGURE 4. Experimental vs dual-impedance model results for fluoranthene- $d_{10}$  desorption from particles.  $D_{a,1} = 1.7 \times 10^{-13} \text{ cm}^2/\text{s}$ ,  $D_{a,2} = 2 \times 10^{-16} \text{ cm}^2/\text{s}$ . (a) Desorption from particles in transfer pipe and stripping device. (b) Desorption from particles in sampling denuder at different residence times. (c) Desorption from particles in sampling denuder at a constant residence time.

times in the transfer pipe of 5.6–25.9 s and residence times in the LGPS of 1.5–7.2 s.

To simulate PAH desorption from particles in the transfer pipe and LGPS, the PAH gas-phase profile as a function of time (i.e., as the aerosol passed through the transfer pipe and LGPS) must be input into the model. This information was obtained using denuder theory in conjunction with experimental data as derived in Appendix 4 (see Supporting Information).

The experimental vs model particle-phase concentrations for fluoranthene- $d_{10}$  in sampling event LGPS2 using the one-layer and dual-impedance models are shown in Figures 2b and 3b, respectively. Note that the dual-impedance model is able to closely reproduce the observed results, while the one-layer model is not able to simulate desorption from particles at these short time scales. A summary of the experimental vs model desorption results for fluoranthene- $d_{10}$  using the dual-impedance model is shown in Figure 4a.

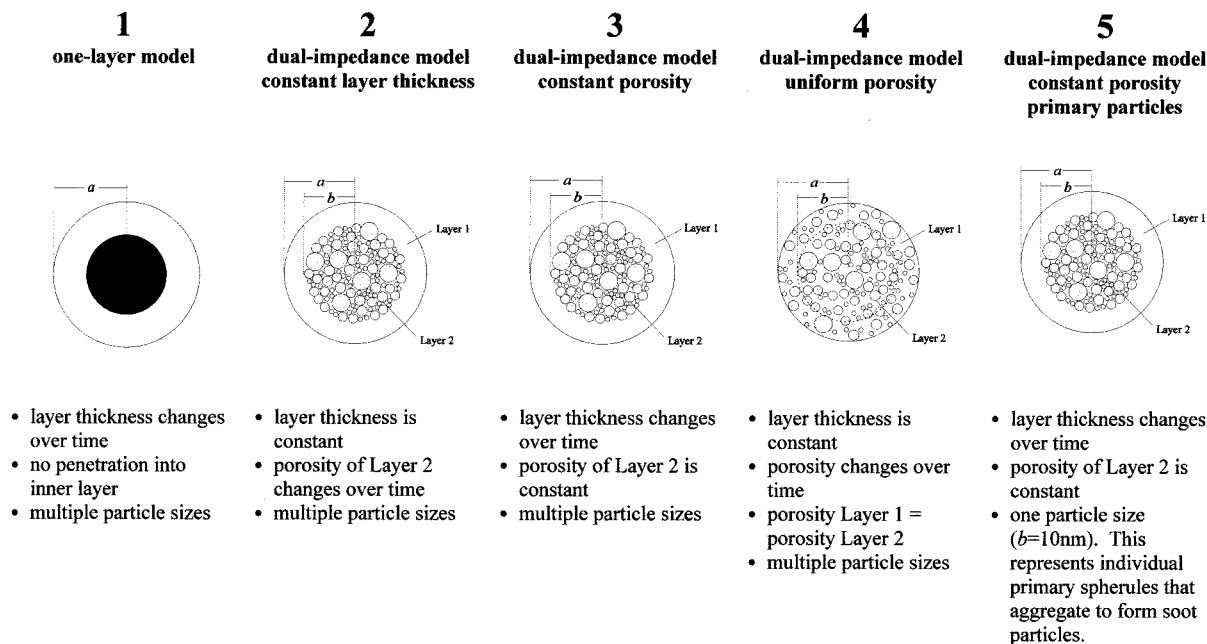


FIGURE 5. Model particles.

As expected, the observed amount of fluoranthene- $d_{10}$  desorbed from the particles increases as the residence time in the transfer pipe and LGPS increases, and the model is able to closely simulate this. At these time scales (5.6–33.1 s), the model is able to optimize on the outer layer apparent diffusion coefficient,  $D_{a,1}$  (e.g.,  $D_{a,1} = 1.7 \times 10^{-13} \text{ cm}^2/\text{s}$  for fluoranthene- $d_{10}$ ).

Figures A3-1b, A3-2b, and A3-3b show select experimental vs model particle-phase concentration results, and Figures A3-1c, A3-2c, and A3-3c summarize the experimental vs model desorption results for fluorene- $d_{10}$ , phenanthrene- $d_{10}$ , and benz[a]anthracene- $d_{12}$ , respectively (see Appendix 3 of Supporting Information). These results show that the quality of the model fits for these compounds is similar to that of fluoranthene- $d_{10}$ .

**Desorption of PAHs from Particles as They Pass through a Sampling Denuder at Different Flow Rates.** For this test, simultaneous DFD and FFD samples were taken from the chamber at three different times (sampling events chamber 5–7 in Table 1). Different flow rates through the DFD system were used for each sampling event to study desorption of PAHs from particles at residence times in the top denuder ranging from 0.18 to 1.13 s. These samples were taken late in the experiment (time = 9.48–11.88 h after soot injection) when the system was close to gas–particle equilibrium, as indicated by the calculated equilibrium particle-phase concentration versus the experimental particle-phase concentration (Figures 2a and 3a). This was done to separate the effect of particle aging, as discussed in the next section, from the effect of residence time in the denuder. The gas-phase analyte concentration profile as the aerosol passed through the sampling denuder was again obtained using denuder theory as derived in Appendix 4 (see Supporting Information). This test was similar to the LGPS test discussed in the previous section, except the time scale for desorption was shorter.

The experimental vs model particle-phase concentrations for fluoranthene- $d_{10}$  in sampling event chamber 5 using the one-layer and dual-impedance models are shown in Figures 2c and 3c, respectively. Note again that the dual-impedance model is able to closely simulate the desorption of fluoranthene- $d_{10}$  from the particles, while the one-layer model cannot. A summary of the experimental vs model desorption results for fluoranthene- $d_{10}$  using the dual-impedance model is shown in Figure 4b. Note that amount of fluoranthene- $d_{10}$

desorbed from the particles increases with residence time in the denuder, as expected, and the model is able to closely simulate this trend. The quality of the model fits for the other deuterated PAHs was generally similar to this. Examples of the results for fluorene- $d_{10}$ , phenanthrene- $d_{10}$ , and benz[a]anthracene- $d_{12}$  are shown in Figures A3-1d, A3-2d, and A3-3d, respectively (see Appendix 3 of Supporting Information).

**Desorption of PAHs from Particles as They Pass through a Sampling Denuder at a Given Flow Rate.** The effects of particle aging on the desorption of PAHs from particles as the aerosol passed through the top denuder of a DFD sampling train was studied by taking simultaneous DFD and FFD samples at six different times over the course of the experiment (sampling events chamber 1–3 and LGPS 1–3 in Table 1). The flow rate through the DFD system was held constant for each sample and resulted in a residence time in the top denuder of  $0.37 \pm 0.1 \text{ s}$ .

A summary of the experimental vs model desorption results for fluoranthene- $d_{10}$  using the dual-impedance model is shown in Figure 4c. Note that as the aerosol ages, less fluoranthene- $d_{10}$  is desorbed from particles. This is because the fluoranthene- $d_{10}$  diffuses deeper and deeper into the particles over time (recall that the particle-phase fluoranthene- $d_{10}$  concentration at  $t = 0$  is zero). Accordingly, it is more easily removed early in the experiment, since it has not diffused as deeply into the particle, and more difficult to remove as the particles age. Note that the dual-impedance model is able to simulate this trend reasonably well. The quality of the model fits for the other deuterated PAHs was generally similar to this.

**Effect of Different Model Particles.** Five different model particles were used in simulations to test the effect of conceptual particle morphology on the quality of the simulation's fit to the experimental data and the effect on the value of the optimized apparent diffusion coefficients. The model particles are shown in Figure 5, and the optimized  $D_a$  values are shown in Table 2.  $D_a$  values were obtained by optimization over each of the simulations for the four tests discussed above (i.e.,  $D_a$  values were optimized to give the best fits for all of the results, such as those shown in Figures 3a and 4 for fluoranthene- $d_{10}$ ). As discussed above, samples could not be collected fast enough from the chamber to resolve the rapid rate of PAH sorption by particles in the first few seconds after soot injection. As such, for the dual-

TABLE 2. Optimized Model Parameters

compound	parameter <sup>a</sup>	model particle				
		1	2	3	4	5
fluorene- <i>d</i> <sub>10</sub>	<i>D</i> <sub>a,1</sub> (cm <sup>2</sup> /s)	4.5 × 10 <sup>-16</sup>	2.4 × 10 <sup>-12</sup>	1.8 × 10 <sup>-12</sup>	1.0 × 10 <sup>-11</sup>	1.1 × 10 <sup>-14</sup>
	<i>D</i> <sub>a,2</sub> (cm <sup>2</sup> /s)	0	4 × 10 <sup>-16</sup>	4 × 10 <sup>-16</sup>	2 × 10 <sup>-16</sup>	2 × 10 <sup>-18</sup>
	ε <sub>p,2</sub>	0	0.28	0.29	b/a = 0.76	0.29
phenanthrene- <i>d</i> <sub>10</sub>	<i>D</i> <sub>a,1</sub> (cm <sup>2</sup> /s)	3.5 × 10 <sup>-16</sup>	6.0 × 10 <sup>-12</sup>	2.2 × 10 <sup>-12</sup>	1.2 × 10 <sup>-11</sup>	1.5 × 10 <sup>-14</sup>
	<i>D</i> <sub>a,2</sub> (cm <sup>2</sup> /s)	0	3 × 10 <sup>-16</sup>	2 × 10 <sup>-16</sup>	1 × 10 <sup>-16</sup>	1 × 10 <sup>-18</sup>
	ε <sub>p,2</sub>	0	0.28	0.29	b/a = 0.76	0.29
fluoranthene- <i>d</i> <sub>10</sub>	<i>D</i> <sub>a,1</sub> (cm <sup>2</sup> /s)	2.2 × 10 <sup>-16</sup>	1.7 × 10 <sup>-13</sup>	1.6 × 10 <sup>-13</sup>	4.1 × 10 <sup>-13</sup>	2.2 × 10 <sup>-15</sup>
	<i>D</i> <sub>a,2</sub> (cm <sup>2</sup> /s)	0	2 × 10 <sup>-16</sup>	7 × 10 <sup>-17</sup>	1 × 10 <sup>-16</sup>	1 × 10 <sup>-18</sup>
	ε <sub>p,2</sub>	0	0.28	0.29	b/a = 0.76	0.29
benz[ <i>a</i> ]anthracene- <i>d</i> <sub>12</sub>	<i>D</i> <sub>a,1</sub> (cm <sup>2</sup> /s)	2.1 × 10 <sup>-16</sup>	1.8 × 10 <sup>-14</sup>	1.6 × 10 <sup>-14</sup>	7.1 × 10 <sup>-14</sup>	1.7 × 10 <sup>-16</sup>
	<i>D</i> <sub>a,2</sub> (cm <sup>2</sup> /s)	0	2 × 10 <sup>-16</sup>	5 × 10 <sup>-17</sup>	6 × 10 <sup>-17</sup>	6 × 10 <sup>-19</sup>
	ε <sub>p,2</sub>	0	0.28	0.29	b/a = 0.76	0.29

<sup>a</sup> ε<sub>p,2</sub> = porosity of layer 2.

impedance models, the desorption tests (Figure 4) primarily dictated the optimized *D*<sub>a,1</sub> values, while the sorption test (Figure 3a) primarily dictated the optimized *D*<sub>a,2</sub> values.

Model particle 1 is the one-layer model that we previously described (19) and was used for the simulations shown in Figure 2. In this model, the carbonaceous core is located at the center of the particle and is not penetrated by the target analytes. Model particle 2 is the dual-impedance model described previously (19) and was used for the simulations shown in Figures 3, 4, A3-1, A3-2, and A3-3. Here, the inner layer (layer 2) is porous and contains all of the solid material in the particle. The porosity of layer 2 changes over time in response to changes in the measured amount of organic material in the particles (i.e., changing *f*<sub>om</sub>) to ensure conservation of mass as detailed by Strommen and Kamens (19). The thickness of the layers does not change over time in this model particle. Model particle 3 is similar to model particle 2 except the porosity of layer 2 remains constant, and the layer thickness is allowed to change with time. In model particle 4, the porosity is uniform throughout the particle. This model was implemented because optimizations using model particles 2 and 3 resulted in *D*<sub>a,1</sub> values on the order of 10<sup>-14</sup>–10<sup>-12</sup> cm<sup>2</sup>/s (Table 2). Since free-liquid diffusion coefficients are normally on the order of 10<sup>-7</sup>–10<sup>-5</sup> cm<sup>2</sup>/s, additional sources of impedance such as tortuosity and adsorption/desorption, which are associated with the presence of solids, must be occurring in the outer layer. Accordingly, this model particle is conceptually more correct than particles 2 and 3. Model particle 5 is the same as model particle 3 except the particles are assumed to be monodisperse with a diameter of 20 nm. This model particle represents the primary spherules that aggregate to form a diesel soot "particle". These spherules have been shown to be nearly monodisperse with a diameter of 20–50 nm depending on formation conditions (34, 35). This model assumes that the microtransport properties of an analyte is the same in an aggregated particle as in the nonaggregated primary spherules. For instance, this assumes that mass transport in the "bridges" connecting primary particles is so fast as to be not rate limiting. Of course, this conceptual model is not entirely correct, because the bridges will offer some diffusional impedance. It does, however, have the advantage of retaining the observed spherical geometry of primary particles, whereas model particles 2–4 uses spherical geometry to represent aggregates of primary particles.

The model fits to the experimental data for each of the dual-impedance models shown in Table 2 were similar in quality to those shown in Figures 3a and 4a–c (again, the fits for the one-layer model were poor). Note, however, that the optimized *D*<sub>a</sub> values are different for the different model particles. As such, the choice of which model particle to use

should be based on which model best represents the observed morphological properties of diesel soot particles. This would favor the use of model particles 4 or 5.

**Sources of Microtransport Impedances.** The results in Table 2 show that the apparent diffusion coefficients obtained via optimization are very small (~10<sup>-19</sup>–10<sup>-11</sup> cm<sup>2</sup>/s) relative to typical free-liquid diffusion coefficients (~10<sup>-5</sup>–10<sup>-7</sup> cm<sup>2</sup>/s). This suggests that PAH microtransport is impeded by additional factors, such as adsorption/desorption to/from solid surfaces and an increase in diffusion distance due to the presence of porous solids that cause restrictions in the diffusion pathway (i.e., tortuosity). The relative magnitude of these impedances is explored in the following calculation and discussion.

A pore-retarded diffusion model in which the analyte diffuses in the liquid-filled pores of the particles is used for this calculation (36). Assuming that partitioning of an analyte between the particle's solids and organic liquid can be described by a linear isotherm and that the adsorption is instantaneous, the apparent diffusion coefficient, *D*<sub>a</sub>, can be related to impedances from (a) free-liquid diffusion, (b) adsorption to solids, and (c) tortuosity by the following expression (37, 38):

$$D_a = \frac{D_l/\tau_e}{1 + \frac{(1 - \epsilon_p)\rho_s K_D}{\epsilon_p}} \quad (6)$$

where *D*<sub>l</sub> is the free-liquid diffusion coefficient (cm<sup>2</sup>/s); τ<sub>e</sub> (= τ/*K*<sub>r</sub>) is the effective tortuosity factor; τ is the tortuosity factor (≥ 1); *K*<sub>r</sub> is the constrictivity factor (≤ 1); *K*<sub>D</sub> (= *C*<sub>s</sub>/*C*<sub>l</sub>) is the distribution coefficient (mL of liquid/g of solid), which quantifies the analyte's equilibrium partitioning between adsorption to solids, *C*<sub>s</sub> (ng/g of solid), and dissolution in the liquid organic material, *C*<sub>l</sub> (ng/mL of liquid); ε<sub>p</sub> is the particle porosity; and ρ<sub>s</sub> is the density of the solids (g/mL). Each of the variables in eq 6, except τ<sub>e</sub>, can be estimated from experimental and modeling results. This provides a method of estimating the effective tortuosity. For example, the effective tortuosity factor in the outer layer of the diesel soot particles using the *D*<sub>a,1</sub> value for fluoranthene-*d*<sub>10</sub> in model particle 4 (Table 2) and the experimental data from the current study at a time of 3 h after diesel soot injection can be calculated using the following data: *D*<sub>a</sub> = 4.1 × 10<sup>-13</sup> cm<sup>2</sup>/s (Table 2); *D*<sub>l</sub> = 1 × 10<sup>-6</sup> cm<sup>2</sup>/s, which is slightly smaller than the value in water (39); and ε<sub>p</sub> = 0.50, the value obtained from the experimental *f*<sub>om</sub> (0.36, measured), estimated ρ<sub>om</sub> [1.19 g/mL, based on the characterization data of Rogge et al. (31)], and the estimated ρ<sub>s</sub> [2.0 g/mL; 32]. The liquid–solid distribution coefficient, *K*<sub>D</sub>, can be calculated from the



experimental equilibrium gas–particle partitioning coefficient,  $K_p$ , and the gas–particle absorption partitioning coefficient,  $K_{p,om}$ . The value of  $K_{p,om}$  can be calculated using the model of Jang et al. (40, 41), which determines an analyte's activity coefficient in the liquid portion of the particle using group contribution theory. Put simply, the overall gas–particle partitioning is controlled by two processes: (a) absorption of analyte in the liquid portion of the particle and (b) adsorption of analyte to the solid portion of the particle (from the liquid portion, given complete coverage of the solid portion by liquid). As such, if the overall gas–particle partitioning (absorption + adsorption) and the adsorptive partitioning are known, the adsorptive partitioning, which is quantified by  $K_D$ , can be calculated. This derivation and example calculation are presented in Appendix 5 (see Supporting Information). For this example, this treatment results in a  $K_D$  value of 0.6 mL of liquid/g of solid. Substitution of these values into eq 6 results in an effective tortuosity factor,  $\tau_e$ , of  $1 \times 10^6$ . The sensitivity of this value to the input parameters was tested by changing each input value over a range of reasonable uncertainties and  $D_a$  values. Changing the value of  $D_l$  by  $\pm 1$  order of magnitude,  $\epsilon_p$  by  $\pm 0.2$ ,  $\rho_s$  by  $\pm 0.4$  g/mL,  $K_D$  by  $\pm 0.6$  mL of liquid/g of solid, and  $D_a$  over all the  $D_{a,1}$  and  $D_{a,2}$  values for model particle 4 in Table 2 results in  $\tau_e$  values ranging from  $1 \times 10^3$  to  $2 \times 10^{11}$ . Furthermore, using  $\tau_e = 1 \times 10^6$ , the calculated value of  $D_a$  only changes from  $4.1 \times 10^{-13}$  cm<sup>2</sup>/s when  $K_D = 0.6$  mL of liquid/g of solid to  $1.0 \times 10^{-12}$  cm<sup>2</sup>/s when  $K_D = 0$  mL of liquid/g of solid (i.e., no adsorption). However, using  $K_D = 0.6$  mL of liquid/g of solid, the calculated  $D_a$  value changes from  $4.1 \times 10^{-13}$  cm<sup>2</sup>/s when  $\tau_e = 1 \times 10^6$  to  $2.4 \times 10^{-7}$  cm<sup>2</sup>/s when  $\tau_e = 2$ . [The value of  $\tau_e = 2$  was obtained using the common assumption that  $\tau_e = 1/\epsilon_p$ , which is derived from the random pore model of Wakao and Smith (42).] Therefore, the high effective tortuosity values at all reasonable input values, the high sensitivity of  $D_a$  values to changes in  $\tau_e$  values, and the low sensitivity of  $D_a$  values to changes in  $K_D$  suggest that tortuosity is a more important factor than adsorption/desorption in impeding the microtransport of these PAHs in diesel soot particles.

Two possible sources of the calculated high effective tortuosities are molecular exclusion and constriction in small pores. Transmission electron microscopy images of diesel soot particles show that a high fraction ( $\geq 95\%$ ) of the interplanar spacings between adjacent carbon layers are in the range of 0.32–0.44 nm (43). Since the calculated critical molecular diameters of the PAHs used in the present study are in the range of 0.7–1.1 nm (44, 45), these compounds would be excluded from most of the pores. Even if the PAHs were able to enter the pores, they may experience hydrodynamic drag as a result of their proximity to the solid walls of the pores (38, 44, 45). Note that these impedances due to molecular exclusion and constriction are included in the effective tortuosity factor,  $\tau_e$ , in eq 6 via changes in the tortuosity factor,  $\tau$ , and the constrictivity factor,  $K_r$ , respectively.

Another potential impedance is restricted diffusion in solidified organic material. The example calculation above assumes that the particle organic material is a liquid. However, given that the organic material that has been identified in diesel soot particles is largely composed of C19–C32 *n*-alkanes and C6–C19 *n*-alkanoic acids (31), it may exist in a partially solidified state at the temperatures of the current study ( $T = 15$ – $10$  °C). In fact, a simplified surrogate diesel soot organic mixture containing C16 and C24 *n*-alkanes; C6, C11, and C16 *n*-alkanoic acids; and benzoic acid, in the mole fractions used by Jang et al. (40, 41) for UNIFAC modeling of diesel soot (C16 *n*-alkane was substituted for C21 *n*-alkane in this mixture) crystallized when cooled below 32.1 °C. Although the freezing point of real diesel soot particle organic

material may vary from that of this simplified solution, these results imply that certain portions of the organic material in diesel soot particles may be crystallized at the temperatures of the current study. Accordingly, the presence of solidified organic material may impede diffusion via additional tortuosity and slow diffusion inside the solid organic matrix.

Only semiquantitative conclusions can currently be drawn regarding the sources of microtransport impedances in diesel soot particles. More rigorous studies involving particle characterization and liquid–solid partitioning are needed to provide a more detailed picture of these processes and to determine the appropriate conceptual particle model.

Note also from Table 2 that the magnitude of the apparent diffusion coefficients decreases as the molecular size of the PAH increases, as expected. The differences in apparent diffusion coefficients between PAHs most likely stems from differences in the factors addressed in the previous discussion: (a) free-liquid diffusivities, (b) solid–liquid adsorption isotherms, (c) constrictivity in small pores, and (d) exclusion from small pores. Each of these factors should result in a decrease in the apparent diffusion coefficient with increasing PAH size. The calculated difference in the free-liquid diffusion coefficient between benz[a]anthracene vs fluoranthene, phenanthrene, and fluorene is only 9%, 15%, and 19%, respectively (see Appendix 6 of Supporting Information for this calculation). Since the apparent diffusion coefficient is proportional to the free-liquid diffusion coefficient (eq 6) and the observed differences in apparent diffusivities between PAHs (Table 2) is significantly larger than this calculated differences in free-liquid diffusivities, the differences in free-liquid diffusivities between PAHs do not appear to significantly contribute to the observed differences in apparent diffusivities. As such, the latter three factors must be responsible for the observed differences.

In summary, we were able to closely simulate experimental sorption and desorption data for four PAHs in airborne diesel soot particles over time scales ranging from hours to fractions of seconds. Furthermore, the resulting apparent diffusion coefficients decreased with increasing PAH molecular size, as expected. These results provide insight into the source of microtransport impedances in diesel soot particles and indicate that a dual-impedance radial diffusion model may be used to accurately simulate microtransport of SOC in diesel soot particles and probably in other types of carbonaceous particles containing a significant organic fraction. This tool may be used for various purposes, such as (a) the inclusion in atmospheric models to simulate nonequilibrium partitioning of SOC between the gas phase and sorption in particulate matter, (b) the quantification of sampling artifacts due to analyte desorption from particles when sampling aerosols with diffusion denuders, and (c) the simulation of SOC desorption from particles in the respiratory system which will affect the calculated analyte deposition pattern.

**Distribution of Model.** The FORTRAN source code and a user's manual for RADDIF, the model used in this study, may be downloaded from <http://airsite.unc.edu>.

## Acknowledgments

This work was supported by grants from the U. S. Environmental Protection Agency through the Science to Achieve Results (STAR) Graduate Fellowship Program and the U.S. National Science Foundation (ATM 9708533, Dr. Ann Marie Schmoltner, Project Officer). We thank Myoseon Jang, Bharadwaj Chandramouli, and Kristin Fletcher for assisting with chamber experiments.

## Supporting Information Available

Six appendices giving the following information: corrections of FFD sampling train data for gas-phase PAH adsorption on



filters; determination of  $K_p$  values; experimental vs simulation results for fluorene- $d_{10}$ , phenanthrene- $d_{10}$ , and benz[a]-anthracene- $d_{12}$ ; calculation of gas-phase PAH concentration as the aerosol passes through the transfer pipe, LGPS, and sampling denuders; calculation of  $K_D$ ; and calculation of the differences in free-liquid diffusion coefficients,  $D_1$ , between PAHs. This material is available free of charge via the Internet at <http://pubs.acs.org>.

## Literature Cited

- Dockery, D. W.; Pope, C. A., III; Xu, X.; Spengler, J. D.; Ware, J. H.; Fay, M. E.; Ferris, B. G., Jr.; Speizer, F. E. *N. Engl. J. Med.* **1993**, *329*, 1753–1759.
- Pope, C. A., III; Thun, M. J.; Namboodiri, M. M.; Dockery, D. W.; Evans, J. S.; Speizer, F. E.; Heath, C. W., Jr. *Am. J. Respir. Crit. Care Med.* **1995**, *151*, 669–674.
- Yamasaki, H. K.; Kawata, Y.; Miyamoto, H. *Environ. Sci. Technol.* **1982**, *16*, 189–194.
- Bidleman, T. F.; Billings, W. N.; Foreman, W. T. *Environ. Sci. Technol.* **1986**, *20*, 1038–1043.
- Bidleman, T. F. *Environ. Sci. Technol.* **1988**, *22*, 361–367.
- Pankow, J. F. *Atmos. Environ.* **1987**, *21*, 2563–2571.
- Scheringer, M. *Environ. Sci. Technol.* **1997**, *31*, 2891–2897.
- Gustafson, K. E.; Dickhut, R. M. *Environ. Sci. Technol.* **1997**, *31*, 140–147.
- Cotham, W. E.; Bidleman, T. F. *Environ. Sci. Technol.* **1995**, *29*, 2782–2789.
- Rao, P. S. C.; Jessup, R. E.; Rolston, D. E.; Davidson, J. M.; Kilcrease, D. P. *Soil Sci. Soc. Am. J.* **1980**, *44*, 684–688.
- Rao, P. S. C.; Jessup, R. E.; Addiscott, T. M. *Soil Sci.* **1982**, *133*, 342–349.
- Miller, C. T.; Weber, W. J., Jr. *Ground Water* **1984**, *22*, 584–592.
- Wu, S.; Gschwend, P. M. *Environ. Sci. Technol.* **1986**, *20*, 717–725.
- Wu, S.; Gschwend, P. M. *Water Resour. Res.* **1988**, *24*, 1373–1383.
- Luthy, R. G.; Aiken, G. R.; Brusseau, M. L.; Cunningham, S. D.; Gschwend, P. M.; Pignatello, J. J.; Reinhard, M.; Traina, S. J.; Weber, W. J., Jr.; Westall, J. C. *Environ. Sci. Technol.* **1997**, *31*, 3341–3347.
- Rounds, S. A.; Pankow, J. F. *Environ. Sci. Technol.* **1990**, *24*, 1378–1386.
- Rounds, S. A.; Tiffany, B. A.; Pankow, J. F. *Environ. Sci. Technol.* **1993**, *27*, 366–377.
- Odum, J. R.; Yu, J.; Kamens, R. M. *Environ. Sci. Technol.* **1994**, *28*, 2278–2285.
- Strommen, M. R.; Kamens, R. M. *Environ. Sci. Technol.* **1997**, *31*, 2983–2990.
- Kamens, R.; Odum, J.; Fan, Z. *Environ. Sci. Technol.* **1995**, *29*, 43–50.
- Kamens, R. M.; Coe, D. L. *Environ. Sci. Technol.* **1997**, *31*, 1830–1833.
- Turpin, B. J.; Huntzicker, J. J.; Hering, S. V. *Atmos. Environ.* **1994**, *28*, 3061–3071.
- McDow, S. R.; Huntzicker, J. J. *Atmos. Environ.* **1990**, *24A*, 2563–2571.
- Gundel, L. A.; Lee, V. C.; Mahanama, K. R. R.; Stevens, R. K.; Daisey, J. M. *Atmos. Environ.* **1995**, *29*, 1719–1733.
- Fan, Z.; Chen, D.; Birla, P.; Kamens, R. M. *Atmos. Environ.* **1995**, *29*, 1171–1181.
- Kirchmer, C. J.; Winter, M. C.; Kelly, B. A. *Environ. Sci. Technol.* **1983**, *17*, 396–401.
- Crank, J. *The Mathematics of Diffusion*, 2nd ed.; Oxford University Press: Oxford, 1975; p 96.
- Pankow, J. F. *Atmos. Environ.* **1991**, *25A*, 2229–2239.
- Brenan, K. E.; Campbell, S. L.; Petzold, L. R. *Numerical Solution of Initial-Value Problems in Differential Algebraic Equations*; Society for Industrial and Applied Mathematics: Philadelphia, 1996.
- Petzold, L. R.; Brown, P. N.; Hindmarsh, A. C.; Ulrich, C. W. *DDASPK (FORTRAN Code)*; U.S. Department of Energy, Center for Computational Sciences & Engineering, L-316, Lawrence Livermore National Laboratory: Berkley, CA, 1995; Contract W-7405-Eng-48.
- Rogge, W. F.; Hildemann, L. M.; Mazurek, M. A.; Cass, G. R.; Simoneit, B. R. T. *Environ. Sci. Technol.* **1993**, *27*, 636–651.
- Ross, M. M.; Risby, T. H.; Steele, W. A.; Lestz, S. S.; Yasbin, R. E. *Colloids Surf.* **1982**, *5*, 17–31.
- Burton, S.; Garbow, K. E.; Hillstrom, J. J. *MINPACK Project (FORTRAN Code)*; Argonne National Laboratory: March 1980.
- Ishiguro, T.; Takatori, Y.; Akihama, K. *Combust. Flame* **1997**, *108*, 231–234.
- Colbeck, I.; Atkinson, B.; Johar, Y. J. *Aerosol Sci.* **1997**, *28*, 715–723.
- Wu, S.; Gschwend, P. M. *Environ. Sci. Technol.* **1986**, *20*, 717–725.
- Weber, W. J., Jr.; DiGiano, F. A. *Process Dynamics in Environmental Systems*; John Wiley & Sons: New York, 1996.
- Ball, W. P.; Roberts, P. V.; *Environ. Sci. Technol.* **1991**, *25*, 1237–1249.
- Schwarzenbach, R. P.; Gschwend, P. M.; Imboden, D. M. *Environmental Organic Chemistry*; John Wiley & Sons: New York, 1993.
- Jang, M.; Kamens, R. M.; Leach, K. B.; Strommen, M. R. *Environ. Sci. Technol.* **1997**, *31*, 2805–2811.
- Jang, M.; Kamens, R. M. *Environ. Sci. Technol.* **1998**, *32*, 1237–1243.
- Wakao, N.; Smith, J. M. *Chem. Eng. Sci.* **1962**, *17*, 825–834.
- Palotás, Á. B.; Rainey, L. C.; Feldermann, C. J.; Sarofim, A. F.; Vander Sande, J. B. *Microsc. Res. Tech.* **1996**, *33*, 266–278.
- Satterfield, C. N.; Colton, C. K.; Pitcher, W. H., Jr. *AIChE J.* **1973**, *19*, 628–635.
- Chantong, A.; Massoth, F. E. *AIChE J.* **1983**, *29*, 725–731.
- Leach, K. B.; Kamens, R. M.; Strommen, M. R.; Jang, M. *J. Atm. Chem.* (in press).
- Yamasaki, H.; Kuwata, K.; Kuge, Y. *Nippon Kagaku Kaishi* **1984**, *8*, 1324–1329.
- Hamilton, D. J. *J. Chromatogr.* **1980**, *195*, 75–83.
- Hinckley, D. A.; Bidleman, T. F.; Foreman, W. T.; Tuschall, J. R. *J. Chem. Eng. Data* **1990**, *35*, 232–237.
- De Santis, F. *Anal. Chem.* **1994**, *66*, 3503–3504.
- Fuller, E. N.; Schettler, P. D.; Giddings, J. C. *Ind. Eng. Chem.* **1966**, *58*, 19–27.
- Pankow, J. F. *Atmos. Environ.* **1994**, *28*, 185–188.
- Wilke, C. R.; Chang, P. C. *AIChE J.* **1955**, *1*, 264–270.
- Perry, R. H.; Chilton, C. H. *Handbook of Chemical Engineering*, 5th ed.; McGraw-Hill Book Company: New York, 1973; pp 3–234.

Received for review October 7, 1998. Revised manuscript received February 23, 1999. Accepted March 2, 1999.

ES981035Q